

BUBBLES AND KNOTS IN THE KINEMATICAL STRUCTURE OF THE BIPOLAR PLANETARY NEBULA NGC 2818

ROBERTO VÁZQUEZ

Instituto de Astronomía, Universidad Nacional Autónoma de México, Km 103 Carretera Tijuana-Ensenada,
22860 Ensenada, B. C., Mexico
vazquez@astro.unam.mx

Submitted to The Astrophysical Journal

ABSTRACT

High-resolution Hubble Space Telescope (HST) archive imaging and high-dispersion spectroscopy are used to study the complex morphological and kinematical structure of the planetary nebula, NGC 2818. We analyze narrow band H α , [O III], [N II], [S II] and He II images, addressing important morphological features. Ground-based longslit echelle spectra were obtained crossing NGC 2818 at five different positions to precisely determine kinematical features in the structure of the nebula. A distance of 2.5 kpc (Van de Steene & Zijlstra 1995) was used to determine physical scales. Constructing models to fit the data with modern computational tools, we find NGC 2818 is composed by: (1) a non-uniform bipolar structure with a semi-major axis of 0.92 pc (75 arcsec), possibly deformed by the stellar wind, (2) a 0.17 pc (14 arcsec) diameter central region, which is potentially the remnant of an equatorial enhancement, and (3) a great number of cometary knots. These knots are preferentially located inside a radius of 0.24 pc (20 arcsec) around the central star. The major axis of the main structure is oriented at $i \simeq 60^\circ$ with respect to the line-of-sight and at PA = $+89^\circ$ on the plane of the sky. Expansion velocities of this nebula are $V_{\text{pol}} = 105 \text{ km s}^{-1}$ and $V_{\text{eq}} = 20 \text{ km s}^{-1}$, which lead to our estimate of the kinematical age of $\tau_k \simeq 8,400 \pm 3,400 \text{ yr}$ (assuming homologous expansion). Our observations do not support the idea that high velocity collimated ejections are responsible for the formation of microstructures inside the nebula. We determine the systemic velocity of NGC 2818 to be $V_{\text{HEL}} = +26 \pm 2 \text{ km s}^{-1}$.

Subject headings: planetary nebulae: individual: NGC 2818 — ISM: kinematics and dynamics

1. INTRODUCTION

1.1. Morphology of Planetary Nebulae

The Planetary Nebula (PN) phase occurs late in the evolution of low-mass stars when UV radiation from the star produces a photoionization-recombination balance in an expanding gaseous shell which had been expelled during the asymptotic giant branch (AGB) phase. Supersonic expansion velocities of 30-40 km s^{-1} are seen in many planetary nebulae (PNe) shells, in which the sound velocity is $\sim 10 \text{ km s}^{-1}$. To explain why the PNe do not follow a free thermal expansion (sound velocity), Kwok, Purton & Fitzgerald (1978) proposed the Interacting Stellar Wind (ISW) model, whereby a denser and slower AGB wind interacts with a new fainter and faster stellar wind. The existence of a fast wind around the central star of PN was confirmed years later by means of UV observations with the International Ultraviolet Explorer (IUE) satellite (e.g. Heap et al. 1978).

Improvements in optical imaging have revealed that an understanding of the morphology of PNe requires more complex explanations and depends on additional physical processes. Balick (1987) proposed a modification to the ISW model, the Generalized Interacting Stellar Wind (GISW) model, which includes an equatorial density enhancement to explain elliptical and bipolar morphologies. This model was subsequently confirmed as an appropriate approximation and further developed by Icke (1988) and Frank & Mellema (1994). Since then, many other morphological features have been discovered in deeper and better resolved observations: open bipolar lobes (called ‘diabolos’; e.g. Monteiro et al. 2000), multipolar structures (e.g.

López et al. 1998; Guerrero & Manchado 1998; Vázquez et al. 2008), rings (e.g. Vázquez et al. 2002; Bond et al. 2003; Mitchell et al. 2006; Jones et al. 2010), and microstructures (also called Low Ionization Structures or LIS) such as ansae, knots, jets and filaments (Gonçalves, Corradi & Mampaso 2001; Miszalski et al. 2009b). In some cases, point-symmetry appears as an additional ingredient to the general morphology (e.g. Guerrero, Vázquez & López 1999; Sabin et al. 2011). As PNe have different observed morphological features, many PNe cannot clearly be assigned membership to a morphological class based on a single defining feature (round, bipolar, or elliptical).

Bipolarity has been explained since the pioneering work of Balick (1987) as a consequence of an equatorial density enhancement of material formed by a mass-loaded ‘superwind’ ejected in the late-AGB phase. However, it is still poorly understood how this superwind is triggered and why it diverges from a spherical ejection. Considering these open questions, De Marco (2009) reviews the possible shaping agents, remarking that binarity (whose definition is expanded to include ‘normal’ stars, brown dwarfs, and even planetary systems, as companions) is a necessary ingredient to explain non-spherical shapes and possibly plays a fundamental role for spherical ones. In particular, De Marco (2009) considers common-envelope binary interactions as an original shaping agent in the formation of bipolar PNe, taking up the work of Soker (1997). Observations to probe binarity in central stars of PNe are non-trivial, but have been successful in a number of cases (e.g. Bond 1979; Bond et al. 1992; Bond 1995, 2000; De Marco et al. 2004; Sorensen & Pollaco 2004; Afşar & Bond 2005) and more recently with different techniques (Miszal-

ski et al. 2008, 2009a; Frew & Parker 2007; Miszalski et al. 2011). A large fraction of PNe have a central star which is actually a close binary system. Miszalski et al. (2009b) note the fraction of close binary systems is $\simeq 17 \pm 5\%$, although there is evidence this number could be higher (De Marco 2009). Currently, the number of close binary systems acting as central stars of planetary nebulae (CSPN) with orbital periods less than one day is ~ 40 (Miszalski et al. 2011).

Scenarios other than a close binary system have also been explored. Numerical simulations demonstrate it is possible to get an equatorial density enhancement in the superwind when stellar rotation and/or magnetic fields are included in the model (García-Segura et al. 1999, 2005). However, other studies have found that stellar differential rotation can be drained by the magnetic field itself (Soker 2006; Nordhaus et al. 2007), reducing the field lifetime to ~ 100 yr, too short to influence the geometry of the gaseous ejecta. More work is needed to determine the extent to which stellar rotation and magnetic fields are important in the formation of single-star axisymmetrical PNe.

To investigate the origin of PNe morphology and to characterize the important physical processes at work, theoretical models need to be supported with more high quality observational data. Morphokinematic studies are a fundamental technique available to approach the problem (Kwok 2000), in which high resolution images and spectra are used to determine the real 3-D form of the complex gaseous structures. In this work we contribute to the study of PNe by modeling the morphokinematic structure of NGC 2818, an object whose highly detailed images have been published in the Hubble Heritage Project website¹.

1.2. NGC 2818

Previous studies of NGC 2818 include the detailed work by Dufour (1984), who analyzed wide band imagery, photoelectric photometry, and optical and IUE spectroscopy. Dufour reports the following physical parameters: $T_e([\text{O III}]) = 14\,500 \pm 500$ K, $T_e([\text{N II}]) = 11\,500 \pm 800$ K, $N_e([\text{S II}]) = 430 \pm 250$ cm⁻³, and $N_e([\text{Cl III}]) = 1300 \pm 800$ cm⁻³, and a heliocentric systemic velocity of $V_{\text{HEL}} = +18.5 \pm 1.7$ km s⁻¹. Schild (1995) obtained infrared images of NGC 2818, in which the central region was clearly seen. This region was more intense in the south, which was suggested to be related to shock excitation.

Phillips & Cuesta (1998) obtained narrow band H α , [O III], [N II], and [S II] images from which some ratios were performed. In spite of the the low resolution of such images, the values of the ratios along the minor axis were plotted in diagnostic diagrams to investigate the nature of the emission. They did not directly observe clumps, but were able to deduce a clumpy medium formed by knots and filaments based on variations in electron density in the [S II] images. They also proposed a possible shock excitation for the southern region along the minor axis seen in H $_2$ by Schild (1995), estimating planar shocks with velocities of $V_s \geq 110$ km s⁻¹. Better resolution H α and [O III] images from Górný et al. (1999) partially show the complex

internal structure proposed by Phillips & Cuesta (1998). A recent study in the *Spitzer* mid-infrared (MIR) bands (3.6, 4.5, 5.8, and 8 μ m) by Phillips & Ramos-Larios (2010) shows gradients in the emission ratios. The observed gradients indicate an increasing importance of emission from photodissociation regions over emission from photoionization. Other contributions to the observed MIR emission include emission from polycyclic aromatic hydrocarbons (PAHs) and effects of shocked regions.

Finally, the study of NGC 2818 is of particular interest because it has been the topic of a series of articles in which its membership to a stellar open cluster is debated. This is an important issue given that distance is a parameter difficult to estimate for PNe, but relatively easy to estimate for stellar clusters. In addition, there are only a few cases of PNe physically related to stellar clusters (e.g. Parker et al. 2011). Addressing this issue is outside the scope of this paper, but a detailed study to address this question is in preparation.

2. OBSERVATIONS AND RESULTS

2.1. Imaging

A series of Hubble Space Telescope (HST) narrow band images, taken with the Wide Field Planetary Camera 2 (WFPC-2), were retrieved from the MAST Archive² to study the apparent morphology of NGC 2818 (proposal ID: 6119; PI: H. E. Bond; Date of observation: 1995 August 26). We show these images in Figure 1, presenting images with different contrasts for [N II] λ 6583 emission (filter F658N) in the two upper panels, H α (left) and [O III] λ 5007 (right) emission lines (filters F656N and F502N) in the central panels, and [S II] λ 6731 (left) and He II λ 4686 (right) emission lines (filters F673N and F469N) in the bottom panels. Three *drizzled* images were combined for each filter in order to remove cosmic rays and bad pixels according to standard procedures in HST reduction manuals.

The appearance of NGC 2818 is slightly different when observed in different filters, as expected due to ionization stratification around the central star of a PN. In Fig. 1, the basic structure appears to be composed of two bipolar lobes, separated in the center by a slightly pinched waist. The enhanced brightness in the cusps of the waist is similar to the limb-brightness of a denser squeezed ring-like structure. We will refer to this area around the central star, clearly seen as the unique emission region in He II, as ‘the central region’.

Both the bipolar lobes and the central region are visible in all panels, with the exception of He II, in which only the central region is visible. We note that the [O III] emission appears to be a smooth distribution of gas, filling the entire nebula. The length of the major axis of the nebula projected on the plane of the sky is $\simeq 101$ arcsec, whereas the minor axis is 31 arcsec, with the smallest separation of 14 arcsec at the cusps of the waist. The whole nebula can be contained in an ellipse of 126×62 arcsec.

In addition to the main structure, a series of microstructures (cometary knots) are especially visible in the [N II] image, but can also be seen in the [S II] and H α images (Fig. 1, left panels). The tails of these cometary knots

¹ <http://heritage.stsci.edu>

² This study is based on observations made with the NASA/ESA HST, obtained from the data archive at the Space Telescope Science Institute (STScI). STScI is operated by the Association of Universities for Research in Astronomy, Inc. under NASA contract NAS 5-26555.

are primarily directed outwards from the geometrical center of the nebula. One of these microstructures, which is very prominent in the central region of the nebula, appears as an asymmetrical and broken ‘big tail’, almost aligned SE-NW. The upper-right panel of Fig. 1 shows a low contrast [N II] image in order to highlight the surroundings of the main structure. At the edges, several tails are also detected that can be traced outwards from the nebula.

We made ratio maps using the HST images (Fig. 1) to emphasize different morphological features in NGC 2818. Fig. 2 shows a mosaic of four image ratios. The upper-left panel shows the [N II]/H α ratio in which the low-ionization regions (white) are better defined than in the original images. The image ratio [O III]/H α is sensitive to the variation of ionization/excitation and chemical abundances (see Corradi et al. 1996) and can also be used to look for signatures of collimated outflows (Medina et al. 2007). Given the nature of the involved ions, the [S II]/H α image ratio is sensitive to shocked regions whereas the He II/H α image ratio shows the very high ionization regions.

The location of the central star of NGC 2818 can be easily found by looking for a hot star in a blue-to-red image ratio. Fig. 3 shows an enlargement of the central region of the nebula in the [O III]/H α image in which the central star appears as a central white dot. The location of the central star is in agreement with the extrapolation of the radial tails of many knots (not shown), as expected if they originate from the identified central star position.

2.2. Longslit high-dispersion spectroscopy

High-dispersion optical spectra were obtained with the Manchester Echelle Spectrometer (MES; Meaburn et al. 2003) and the 2.1 m (f/7.5) telescope at the OAN-SPM³ observatory during 2009 February 4–6. A SITe CCD with 1024×1024 pixels was used as detector. The slit length is 6'5 and the width was set to 150- μ m (2"). A 2×2 binning was used, leading to a spatial scale of 0'6 pixel⁻¹ and a spectral scale of 0.1 Å pixel⁻¹. This spectrograph has no cross dispersion, consequently a $\Delta\lambda = 90$ Å bandwidth filter was used to isolate the 87th order covering the spectral range which includes H α and [N II] λ 6583 emission lines. The spectra were wavelength calibrated with a Th-Ar arc lamp to an accuracy of ± 1 km s⁻¹. The FWHM of the arc lamp emission lines was measured to be $\simeq 12$ km s⁻¹. Spectra were obtained by positioning the slit across five different regions of the nebula, as shown in Figure 4. The position angles (PAs) for these slits are +89° (slit 1), +123° (slit 2), and -1° (slits 3, 4, and 5). Exposure time for all the slits was 1800 s. Seeing was ~ 2 arcsec during observations.

Fig. 5 shows the Position-Velocity (PV) maps for H α (upper panels) and [N II] λ 6583 (lower panels) emission lines. Each column is labeled with the corresponding slit number. We note that the He II λ 6560 line is also observed in the PV maps for slits 1, 2, and 4, in agreement with the highest excitation location shown in the He II image (see lower-right panel in Fig. 1). The relative position is measured with respect to the position of the central star (for slits 1, 2, and 4) and to the major axis defined by slit 1 (for slits 3 and 5). Radial velocity is relative to the systemic

velocity $V_{\text{HEL}} = +26 \pm 2$ km s⁻¹ ($V_{\text{LSR}} = +11 \pm 2$ km s⁻¹). This value was deduced as the mean velocity of the two components of the splitting of the spectral lines, taken from the slit region crossing the central star (on slits 1, 2, and 4). This method only can be done if the splitting of the spectral lines can be measured; that is, when we have high-resolution spectra. It has better accuracy than only taking the maximum of a broad unique emission line, as can be seen in low-resolution spectra. Observing without enough spectral resolution to see the splitting can result in a wrong estimate for the systemic velocity if, as in this case, the components of the splitting have different brightness. Without high resolution spectroscopy, the non-resolved splitting is seen as a broad emission line with its maximum being biased towards the wavelength of the brightest component. Previous determinations of the systemic velocity of NGC 2818 have been affected by low resolution spectra (e.g., $V_{\text{hel}} = 18.5 \pm 1.7$ km s⁻¹, Dufour 1984). In this paper, we present the first systemic velocity determination from the splitting method, utilizing high resolution spectroscopy.

3. DISCUSSION

3.1. The morpho-kinematic structure of NGC 2818

As described above (Sec. 2.1), our inspection of the unprecedented high resolution HST images indicates that NGC 2818 is a morphologically rich PN with minor bubbles, asymmetrical outflows, and cometary knots inside its main structure (Figs. 1 and 2). In a first attempt to study the morphology and kinematics of NGC 2818, we have constructed some simple models using the interactive software SHAPE (Steffen et al. 2011), a computational tool for the morpho-kinematic modeling and reconstruction of astrophysical objects. The internal library of SHAPE includes basic structures such as spheres, cylinders, and tori, which can be modified by applying different parameters and/or functions (“modifiers”). Each structure is composed of a grid in which a certain number of points are distributed. The user defines the number of points for each structure and the volume or surface distribution. Physical parameters, such as density and velocity, can be assigned to the points either as an analytical function or interactively. Several recent papers have used SHAPE to get the structure of PNe (e.g. Miszalski et al. 2011; Hsia et al. 2010; Jones et al. 2010; Contreras et al. 2010). In our particular case, we obtained a final nebula model which fits the main structure of NGC 2818 for both imaging and spectroscopy (Fig. 6). We find NGC 2818 can be modeled as a bipolar structure with major and minor axis length of 1.8×0.3 pc (150×28 arcsec at a distance of 2.5 kpc, following Van de Steene & Zijlstra 1995), with an inclination angle of the major axis equal to 60° with respect to the line of sight (eastern lobe is blueshifted, western lobe is redshifted). The polar and equatorial velocities are $V_{\text{pol}} = 105$ km s⁻¹ and $V_{\text{eq}} = 20$ km s⁻¹, respectively, assuming homologous velocity expansion ($V \propto r$). The shell has a maximum thickness of 0.1 pc ($\simeq 9$ arcsec) becoming thinner towards the poles. Using these velocities and dimensions, we have estimated a kinematical age of $\tau_k \simeq 8,400 \pm 3,400$ yr, which is similar to the age of other PNe with cometary knots in

³ The Observatorio Astronómico Nacional at the Sierra de San Pedro Mártir (OAN-SPM) is operated by the Instituto de Astronomía of the Universidad Nacional Autónoma de México

their morphology (see O’Dell et al. 2002).

The relatively high uncertainty in the kinematical age estimate merits a more detailed explanation. Distance estimates for PNe remain an important issue, given the very few cases in which we can get a ‘direct’ measurement (e.g. via stellar parallax). We have avoided distance estimates for NGC 2818 based on membership of this object to the stellar cluster mentioned in Sec. 1.2, and instead have used statistical values. There are some estimates for the distance to this object ranging from 1.79 kpc (Phillips 2004) to 3.05 kpc (Zhang 1995). Van de Steene & Zijlstra (1995) give a value of 2.5 kpc, which is very close to mean value of the distance range. An uncertainty of $\sim 40\%$ is obtained utilizing the statistical estimates (which covers all the range of distance estimates). Thus, the propagation of this high uncertainty has effects in the same proportion over the physical size (1.8 ± 0.7 pc in the major axis) and the kinematical age ($8,400 \pm 3,400$ yr). Having better distance estimates will improve the accuracy on these two parameters, and is the focus of future work.

Because of their faintness, kinematics from the microstructures cannot be determined as they are not seen in our spectra, with the exception of the ‘big tail’ mentioned in Sec. 2.1. A careful analysis of images in Figs. 1, 2, and 3, as well as the PV map in Fig. 5 (panel 2, lower) indicates that the ‘big tail’, as well as the other similar structures, have the same nature as the rest of the smaller cometary knots, being possibly photoevaporated, blown, and ionized by the action of the wind and radiation from the central star over the dense clumps that remain in its surroundings. In the ‘big tail’ a collimated ejection is unlikely as the two NW pieces do not share the same kinematic behavior, as would be expected in the case of a collimated ejection (see Fig. 5, panel 2, lower). If the ‘big tail’ is not taken into account, it is remarkable to note that the small cometary knots have no apparent preferred direction, whereas the denser and larger features are related to the central region. The latter seems to be similar to the case of the Helix nebula (Meaburn et al. 1998), which has been proposed to have a knotty torus whose axis is seen at 37° with respect to the line of sight.

Finally, the cometary knot antipodes in the upper-left side of the central region of NGC 2818 appear to point towards a kind of ‘local’ bubble center instead of the central star. One possible interpretation is that the peculiar kinematics of several bubbles inside the nebula play an important role in the production of tails. We think that this idea deserves more attention in theoretical studies and is beyond the scope of the present work.

3.2. The evolution of NGC 2818

In this section we consider the line ratio images and what these ratios can tell us about the evolution of NGC 2818. First, we examine the image ratio $[\text{O III}]/\text{H}\alpha$. This ratio is sensitive to the variation of ionization/excitation and chemical abundances (see Corradi et al. 1996) and can also be used to look for signatures of collimated outflows (Medina et al. 2007). According to Medina et al. (2007), PNe with $[\text{O III}]/\text{H}\alpha$ ratios enhanced in an outer layer (or ‘skin’), are related to both, fast collimated outflows and multiple-shells, the latter may even have FLIERs (Fast Low-Ionization Emission Regions; Balick 1987). However,

as seen in Fig. 2 (upper-right panel), NGC 2818 has a $[\text{O III}]/\text{H}\alpha$ ratio diminished (Medina’s type C), which could correspond to either young or evolved PNe, but not related to jets, shocks, or multiple shells. It is important to note that no correction for extinction was applied. In particular, this ratio image could be more affected by interstellar extinction (or internal extinction, including internal small-scale variations) than the other ratios, given the relative large difference between the wavelengths of $[\text{O III}]$ and $\text{H}\alpha$.

The $[\text{S II}]/\text{H}\alpha$ image ratio (Fig. 2, lower-left panel) is sensitive to the shocked regions and is enhanced in the most noticeable tails seen in $[\text{N II}]$. These could indicate either that these tails are shocked gas or that gas in the tails is being shocked by the stellar wind. Following the homologous velocity assumption, we expect no more than 28 km s^{-1} in stellar wind velocity at the distances in which the cometary knots are found, as they are preferentially located at a radius of 20 arcsec around the central star (0.24 pc, assuming a distance of 2.5 kpc). However, these low velocity shocks could be enough to give rise to the $[\text{S II}]/\text{H}\alpha$ ratio in a detectable way (see Phillips & Guzmán 1998, and references therein). The same ratio also appears to exist in the ring zone. This could be in agreement with the results of Schild (1995) and Phillips & Cuesta (1998) who detect emission possibly related to shocked gas. It is also remarkable that based on the imaging in their study, Phillips & Cuesta (1998) propose velocities of 110 km s^{-1} for the farthest regions of the nebula. Based on kinematics, we also estimate polar velocities around this value.

The $\text{He II}/\text{H}\alpha$ image ratio shows the very high ionization regions. As expected, the highest ionized regions in NGC 2818 are enclosed inside the main structure of the nebula in the regions surrounding the central star. This can also be seen in the $[\text{O III}]$ and He II images. In previous sections we defined the ‘central region’ based on the He II emission, whose appearance reminds one of the remnant of an equatorial structure. A possible interpretation of the data could be that NGC 2818 is a bipolar PN whose equatorial density enhancement can be traced by the cusps aligned with the central star and the brightness of the central region. The distorted internal structure and the presence of multiple bubbles and non-uniform microstructures can be seen as part of a pre-existent clumpy medium in the surroundings. Although a definite model for the formation of cometary knots has not been generally accepted, hydrodynamical instabilities appear to adequately explain them (e.g. Capriotti & Kendall 2006). Such instabilities could be formed in the beginning of the proto-PN phase and appear as cometary knots once the bipolar outflow is free. Trying to understand the energetics involved in the whole process of formation and evolution of this nebula is an interesting way to address the study of the synergy between macro- and microstructures in the morphology of PNe.

4. CONCLUSIONS

We have conducted an observational study of NGC 2818 using archival high resolution space-based imaging and high dispersion Earth-based longslit spectroscopy. We derive a systemic velocity of $V_{\text{HEL}} = +26 \pm 2 \text{ km s}^{-1}$. The computational software SHAPE was used to construct a

model to fit our data and improve our interpretation of the overall morphokinematic structure of NGC 2818. Our model is consistent with a bipolar nebula with a semi-major axis of 0.92 pc, possibly deformed by the stellar wind, a 0.17 pc diameter central region that is a potential remnant of an equatorial enhancement, and a great number of cometary knots preferentially located inside a radius of 0.24 pc around the central star. The major axis of the main structure is oriented at $i \simeq 60^\circ$ with respect to the line-of-sight and at PA = $+89^\circ$ on the plane of the sky. Deprojected velocities correspond to an expansion of $V_{\text{pol}} = 105 \text{ km s}^{-1}$ and $V_{\text{eq}} = 20 \text{ km s}^{-1}$, which lead to an estimate of the kinematical age of $\tau_k \simeq 8,400 \pm 3,400 \text{ yr}$. Cometary knots could be related to hydrodynamical instabilities formed before the bipolar outflow started.

This project was supported by UNAM-PAPIIT grants

IN111903 and IN109509. The author is grateful to the anonymous referee for his valuable comments and to his research group “Planetosos” for its support and fruitful discussions, in particular to Mr. Paco Beretta for calling my attention to this object. W. Steffen and L. Guitérrez provided SHAPE and HST advising, respectively. The author also acknowledges the OAN staff at San Pedro Mártir, with special mention to Mr. Gustavo Melgoza-Kennedy (aka “Tiky”) for support during observations. The author is deeply grateful to Dr. Ashley Zauderer for a kind and careful revision of the manuscript. Finally, the author would like to dedicate this paper in memory of Prof. Yolanda Gómez, who was an active researcher in the field of Planetary Nebulae and an indefatigable impeller of science education and outreach, and who recently passed away.

Facilities: HST (WFPC2), SPM (MEZCAL).

REFERENCES

- Acker, A. 1978, *A&AS*, 33, 367
 Afşar, M., Bond, H. E. 2005, *Mem. Soc. Astron. Italiana*, 76, 608
 Balick, B. 1987, *AJ*, 94, 671
 Bonatto, C., Bica, E., Santos Jr., J. F. C. 2008, *MNRAS*, 386, 324
 Bond, H. E. 1979, in *IAU Colloq. 53, White Dwarfs and Variable Degenerate Stars*, ed. H. M. van Horn & Weidemann, 266-268
 ———. 1995, in *Annals of the Israel Physical Society, Asymmetrical Planetary Nebulae*, Vol. 11, ed. A. Harpaz & N. Soker, 61
 ———. 2000, in *ASP Conf. Ser. 199, Asymmetrical Planetary Nebulae II: From Origins to Microstructures*, ed. J. H. Kastner, N. Soker, & S. Rappaport (San Francisco: ASP), 115
 Bond, H. E., Ciardullo, R., Meakes, M. G. 1992, in *IAU Symp. 151, Evolutionary Processes in Interacting Binary Stars*, ed. Y. Kondo, R. Sistero, & R. S. Polidan, 517
 Bond, H. E., Pollacco, D. L., Webbink, R. F. 2003, *AJ*, 125, 260
 Capriotti, E. R., Kendall, A. D. 2006, *ApJ*, 642, 923
 Connolly, L. P. 1977, *PASP*, 89, 528
 Contreras, M. E., Vázquez, R., Miranda, L. F., Olguín, L., Zavala, S., Ayala, S. 2010, *AJ*, 139, 1426
 Corradi, R. L. M., Manso, R., Mampaso, A., Schwarz, H. E. 1996, *A&A*, 313, 913
 De Marco, O. 2009, *PASP*, 121, 316
 De Marco, O., Bond, H. E., Harmer, D., Fleming, A. J. 2004, *ApJ*, 602, L93
 Dufour, R. J. 1984, *ApJ*, 287, 341
 Durand, S., Acker, A., Zijlstra, A. 1998, *A&AS*, 132, 13
 Frank, A., Mellema, G. 1994, *ApJ*, 430, 800
 Frew D. J., Parker Q. A., 2007, in *Corradi R. L. M., Manchado A., Soker N., eds, APN4 Conf. Proc., Asymmetrical Planetary Nebulae IV*, p. 475, available at: <http://www.iac.es/proyecto/apn4/media/pdf/Tfrew.pdf>
 García-Segura, G., Langer, N., Różyczka, M., Franco, J. 1999, *ApJ*, 517, 767
 García-Segura, G., López, J. A., Franco, J. 2005, *ApJ*, 618, 919
 Gonçalves, D. R., Corradi, R. L. M., Mampaso, A., 2001, *ApJ*, 547, 302
 Górny, S. K., Schwarz, H. E., Corradi, R. L. M., Van Winckel, H. 1999, *A&AS*, 136, 145
 Guerrero, M. A., Manchado, A. 1998, *ApJ*, 508, 262
 Guerrero, M. A., Vázquez, R., López, J. A. 1999, *AJ*, 117, 967
 Heap, S. R. et al. 1978, *Nature*, 275, 385
 Hsia, C.-H., Kwok, S., Zhang, Y., Koning, N., Volk, K. 2010, *ApJ*, 725, 173
 Icke, V. 1988, *A&A*, 202, 177
 Jones, D., Lloyd, M., Mitchell, D. L., Pollacco, D. L., O’Brien, T. J., Vaytet, N. M. H. 2010, *MNRAS*, 401, 405
 Kohoutek, L., Roth-Höppner, M. L., Laustsen, S. 1986, *A&A*, 162, 232
 Kwok, S. 2000, *The Origin and Evolution of Planetary Nebulae* (Cambridge Astrophysics Series 31; Cambridge: Cambridge Univ. Press)
 Kwok, S., Purton, C. R., Fitzgerald, P. M. 1978, *ApJ*, 219, L125
 López, J. A., Meaburn, J., Bryce, M., Holloway, A. J. 1998, *ApJ*, 493, 803
 Majaess, D. J., Turner, D. G., Lane, D. J. 2007, *PASP*, 119, 1349
 Meaburn, J., Clayton, C. A., Bryce, M., Walsh, J. R., Holloway, A. J., Steffen, W. 1998, *MNRAS*, 294, 201
 Meaburn, J., López, J. A., Gutiérrez, L., Quirós, F., Murillo, J. M., Valdés, J., Pedráyes, M. 2003, *RevMexAA*, 39, 185
 Meatheringham, S. J., Wood, P. R., Faulkner, D. J. 1988 *ApJ*, 334, 862
 Medina, J. J., Guerrero, M. A., Luridiana, V., Miranda, L. F., Riera, A., Velázquez, P. F. 2007 in *Asymmetrical Planetary Nebulae IV*, R. L. M. Corradi, A. Manchado & N. Soker (eds). Published online at <http://www.iac.es/proyecto/apn4>, p. 235
 Mermilliod, J.-C., Clariá, J. J., Andersen, J., Piatti, A. E., Mayor, M. 2001, *A&A*, 375, 30
 Miszalski, B., Acker, A., Moffat, A. F. J., Parker, Q. A. & Udalski, A. 2008, *A&A*, 488, L79
 ———. 2009a, *A&A*, 496, 813
 Miszalski, B., Acker, A., Parker, Q. A., Moffat, A. F. J. 2009b, *A&A*, 505, 249
 Miszalski, B., Corradi, R. L. M., Boffin, H. M. J., Jones, D., Sabin, L., Santander-García, M., Rodríguez-Gil, P., Rubio-Díez, M. M. 2011, *MNRAS*, 413, 1264
 Mitchell, D. L., Pollacco, D., O’Brien, T. J., Bryce, M., López, J. A., Meaburn, J. 2006 in *Planetary Nebulae in our Galaxy and beyond IAU Symp. 234*, M. J. Barlow & R. H. Méndez (eds). Cambridge University Press, pp. 139-144
 Monteiro, H., Morisset, C., Gruenwald, R., Viegas, S. M. 2000, *ApJ*, 537, 853
 Nordhaus, J., Blackman, E. G., Frank, A. 2007, *MNRAS*, 376, 599
 O’Dell, C. R., Balick, B., Hajian, A. R., Henney, W. J., Burkert, A. 2002, *AJ*, 123, 3329
 Parker, Q. A., Frew, D. J., Miszalski, B., Kovacevik, A. V., Frinchaboy, P. M., Dobbie, P. D., Köpen, J. 2011, *MNRAS*, 413, 1835
 Perek, L., Kohoutek, L. 1967, *Catalog of Galactic Planetary Nebulae* (Prague: Czechoslovakian Academy of Sciences)
 Phillips, J. P. 2004, *ApJS*, 139, 199
 Phillips, J. P., Cuesta, L. 1998, *A&AS*, 133, 381
 Phillips, J. P., Guzmán, V. 1998, *A&AS*, 130, 465
 Phillips, J. P., Ramos-Larios, G. 2010, *MNRAS*, 405, 2179
 Pottasch, S. R. 1983, in *Planetary Nebulae*, ed. D. R. Flower (Reidel, Dordrecht), IAU Symp. 103, 391
 Sabin, L., Vázquez, R., Contreras, M. E., Zavala, S., Olguín, L., Guillén, P. F. 2011 in *Asymmetrical Planetary Nebulae V*, A. A. Zijlstra, F. Lykew, I. McDonald & E. Lagadec (eds.), Publisher: Jodrell Bank Centre for Astrophysics, Manchester, UK, pp. 109-112
 Schild, H. 1994, *A&A*, 297, 246
 Schneider, S. E., Terzian, Y., Purgathofer, A., Perinotto, M. 1983, *ApJS*, 52, 399
 Soker, N. 1997, *ApJS*, 112, 487
 ———. 2006, *ApJ*, 640, 966
 Sorensen, P., Pollaco, D. 2004, in *ASP Conf. Ser. 313, Asymmetrical Planetary Nebulae III*, ed. M. Meixner, J. H. Kastner, B. Balick, & N. Soker (San Francisco: ASP), 494
 Steffen, W., Koning, N., Wenger, S., Morisset, C., Magnor, M. 2011, *IEEE Transactions on Visualization and Computer Graphics*, 17, 454
 Tifft, W. G., Connolly, L. P., Webb, D. F. 1972, *MNRAS*, 158, 47
 VandenBerg, D. A. 1985, *ApJS*, 58, 711
 Van de Steene, G. C., Zijlstra, A. A. 1995, *A&A*, 293, 541
 Vázquez, R., Miranda, L. F., Torrelles, J. M., Olguín, L., Benítez, G., Rodríguez, L. F., López, J. A. 2002, *ApJ*, 576, 860
 Vázquez, R., Miranda, L. F., Olguín, L., Ayala, S., Torrelles, J. M., Contreras, M. E., Guillén, P. F. 2008, *A&A*, 481, 107
 Zhang, C. Y. 1995, *ApJS*, 98, 659

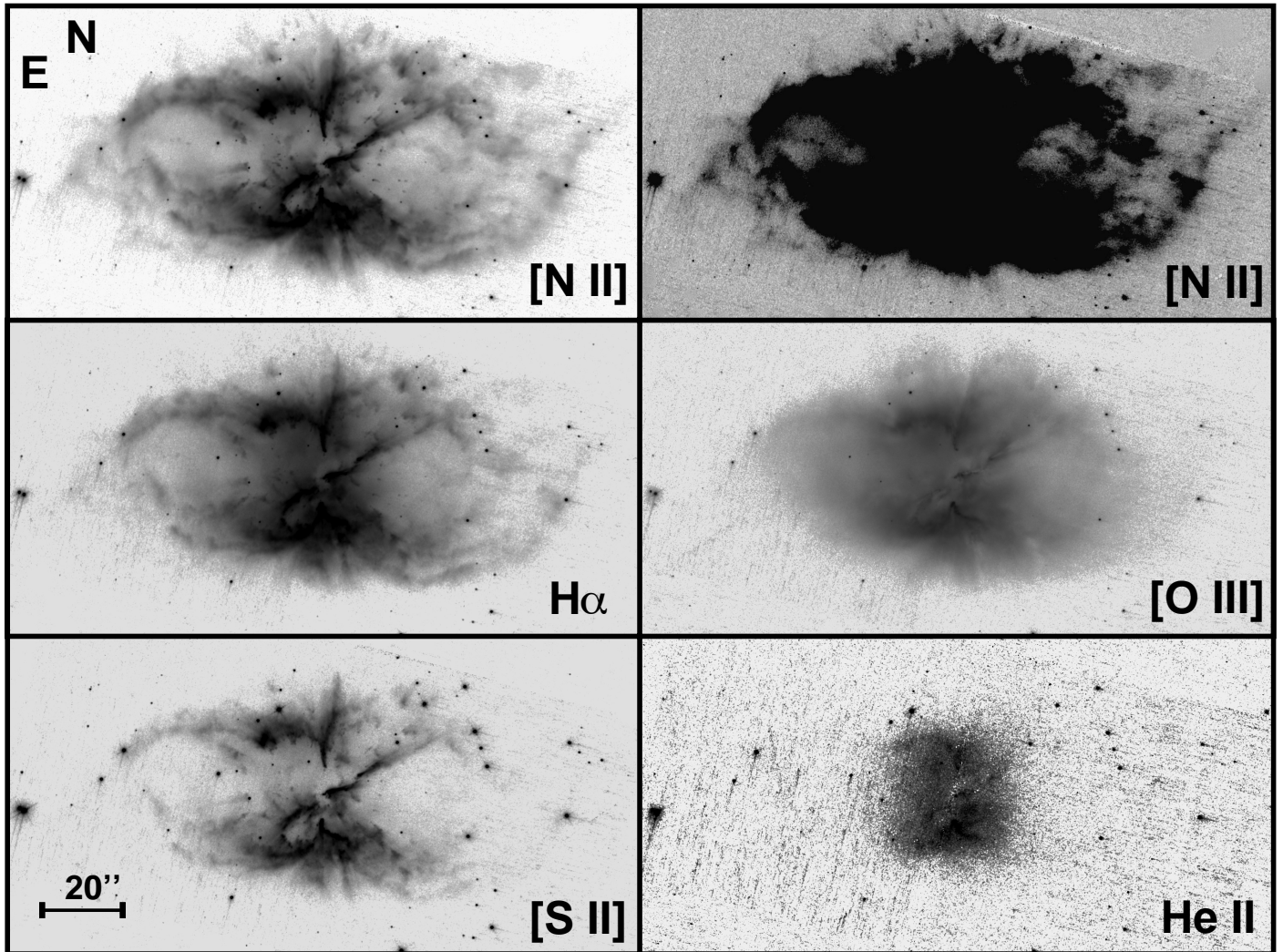


FIG. 1.— HST-WFPC2 narrow band images. Upper panels: [N II] λ 6583 (filter F658N) with two different contrasts; central panels: H α (left; filter F656N) and [O III] λ 5007 (right; filter F502N); lower panels: [S II] λ 6731 (left; filter F673N) and He II λ 4686 (right; filter F469N). Spatial scale is indicated. Sky orientation (north up, east left) is the same in all subsequent figures.

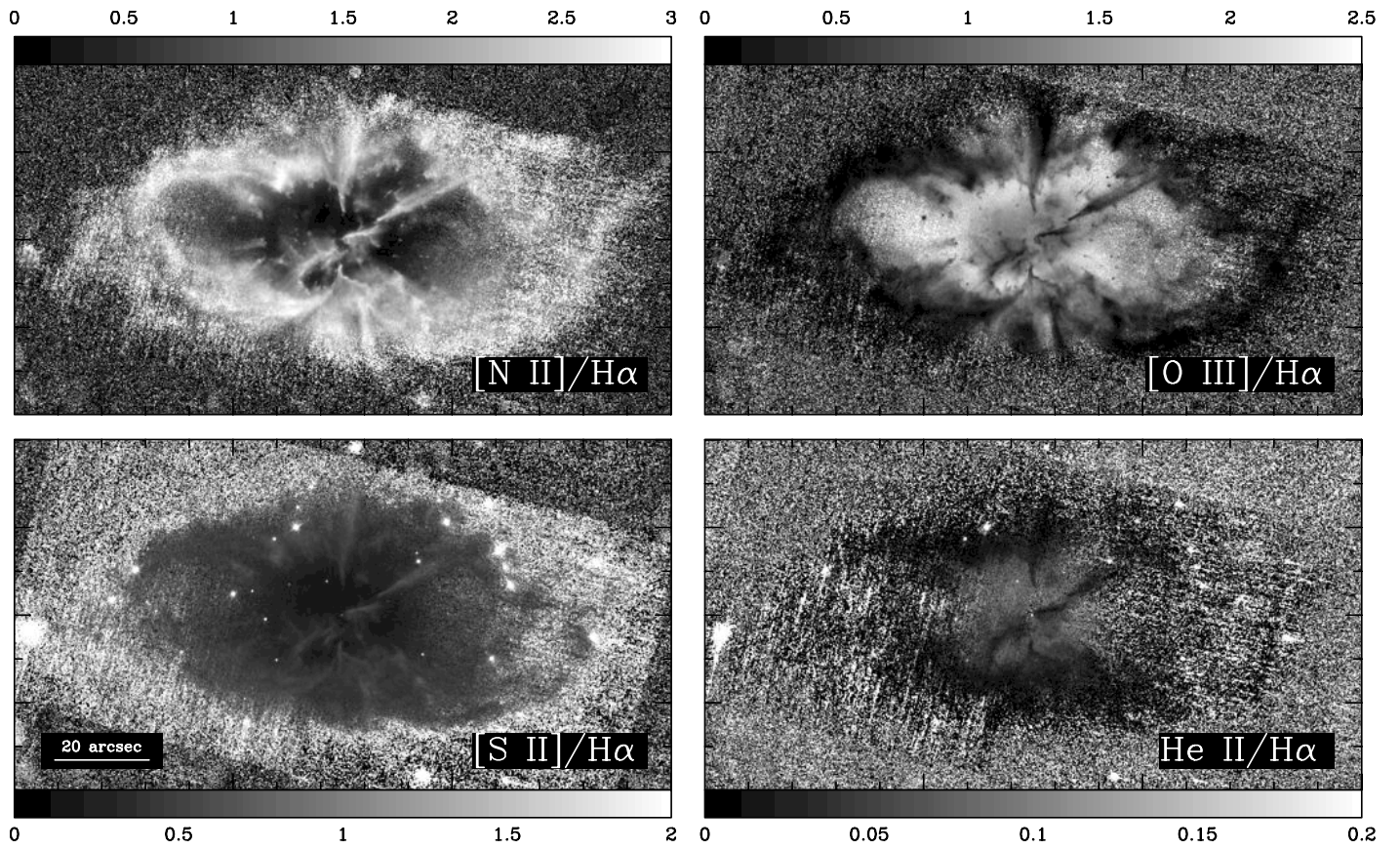


FIG. 2.— HST-WFPC2 narrowband image ratios of NGC 2818. White corresponds to large values of each ratio, indicated by the gray-scale bar. Upper left: $[N II]/H\alpha$. Upper right: $[O III]/H\alpha$. Lower left: $[S II]/H\alpha$. Lower right: $He II/H\alpha$.

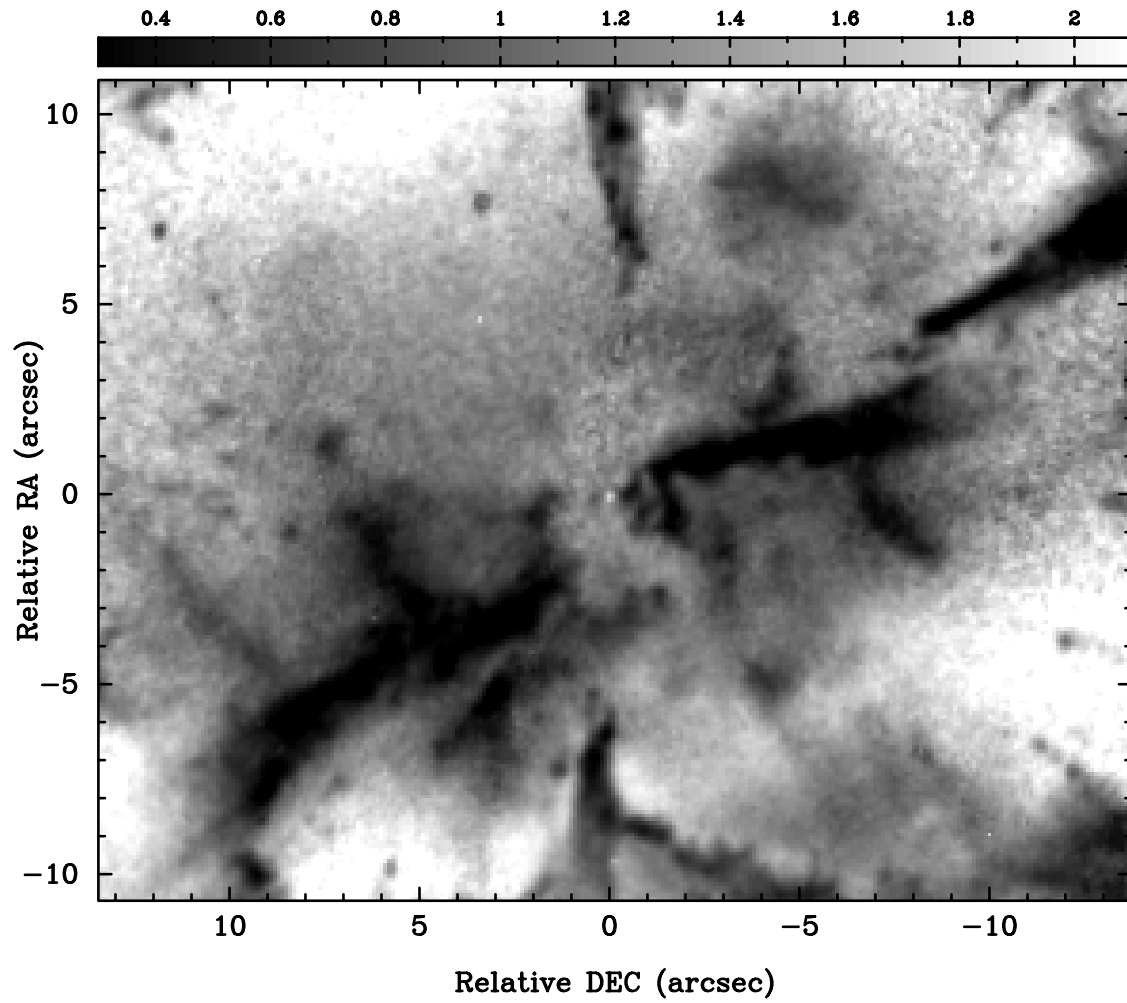


FIG. 3.— Detailed view of the central region in the $[\text{O III}]/\text{H}\alpha$ image ratio presented in Fig. 1. The central white dot corresponds to the central star of NGC 2818.

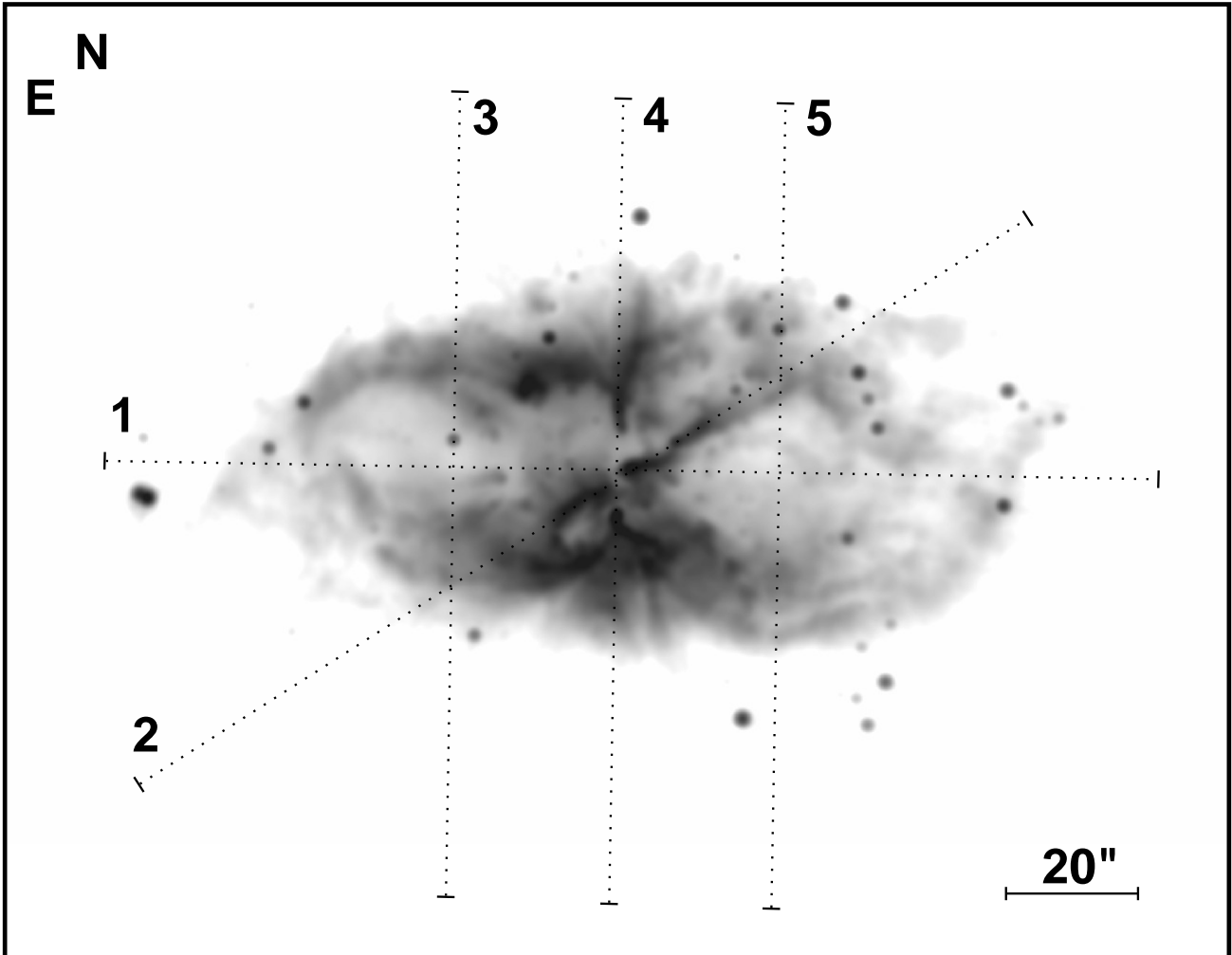


FIG. 4.— Slit positions used in the high dispersion spectroscopy superimposed on an [N II] HST image. PAs= $+89^\circ$ (1), $+123^\circ$ (2), and -1° (3, 4, and 5). The image was gaussian filtered to reproduce the spatial resolution observed in the spectra.

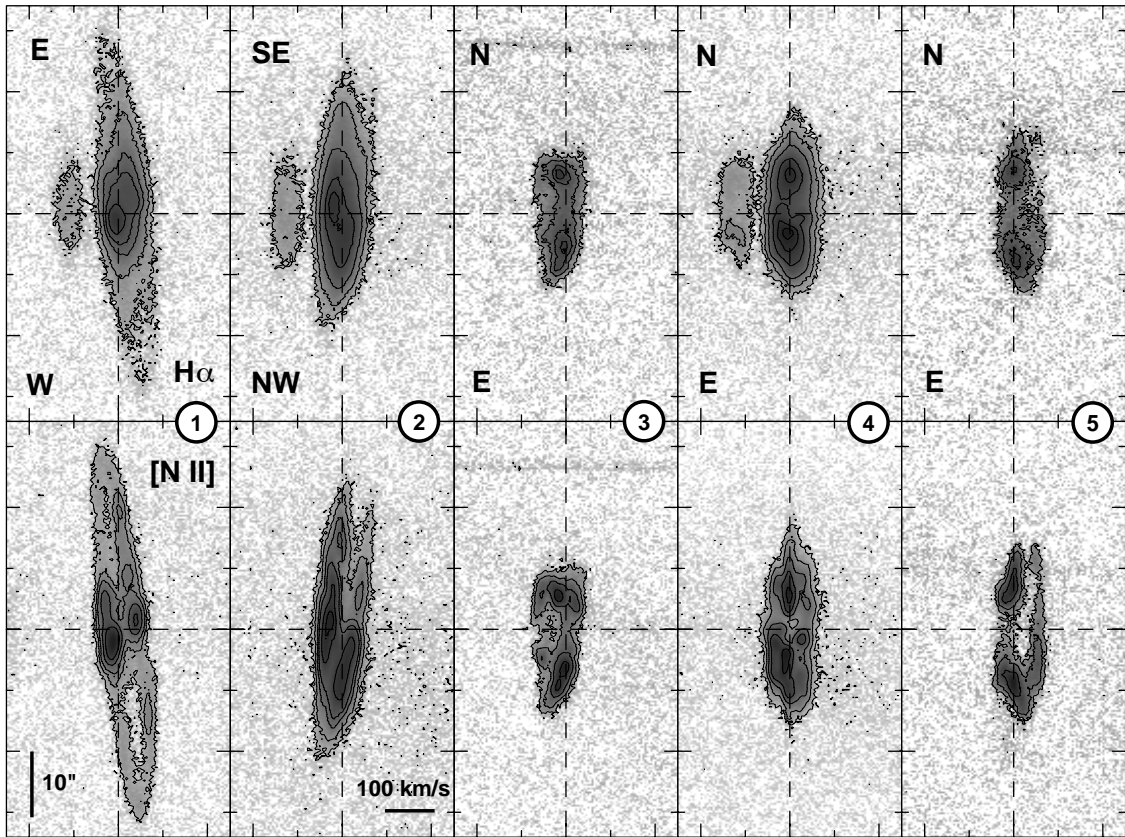


FIG. 5.— Position-Velocity maps of NGC 2818 for slits positions 1 to 5. Upper panels correspond to $H\alpha$, and lower panels to $[\text{N II}] \lambda 6583$. The slit orientation indicated in the upper panels is valid for the two maps in each column. The horizontal dashed lines represent the position of the central star for slits 1, 2, and 4, and the location where slits cross the major axis for slits 4 and 5. The horizontal dashed line corresponds to the systemic radial velocity ($V_{\text{HEL}} = +26 \pm 2 \text{ km s}^{-1}$).

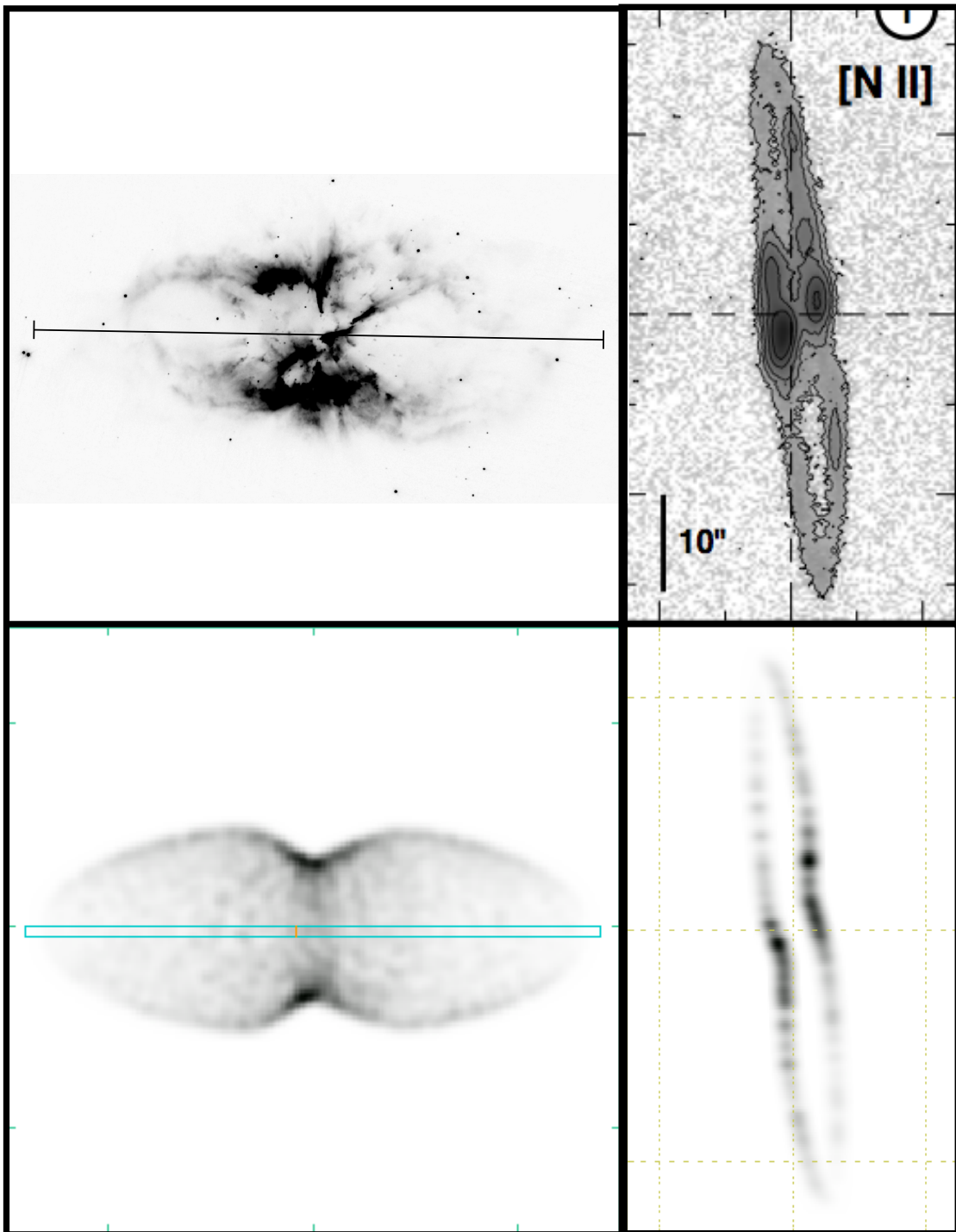


FIG. 6.— Comparison of observed data and the 3D model obtained from SHAPE. Left: Observed [N II] image (upper panel) and the SHAPE image (lower panel). Right: Observed PV map of the [N II] $\lambda 6583$ line at slit position 1 (upper panel) and the corresponding SHAPE synthetic PV map (lower panel).